ISSN: 2692-5397
DOI: 10.33552/MCMS.2022.04.000597
Modern Concepts in Material Science
Iris Publishers

Research Article

Microwave-Induced Attractive Force Between Dielectric Spheres-A Potential Non-Thermal Effect in Microwave Sintering

Li-Chung Liu, Ming-Syun Lin and Kwo Ray Chu*

Department of Physics, National Taiwan University, Taiwan

***Corresponding author:** Kwo Ray Chu, Department of Physics, National Taiwan University, Taipei 106, Taiwan.

Received Date: July 11, 2022

Published Date: July 28, 2022

Abstract

We present a detailed analysis of the polarization-charge buildup and electric-field intensification between two dielectric spheres under microwave radiation, with an emphasis on the resulting attractive force between the spheres. The study is motivated by an outstanding issue in microwave sintering of powder compacts. Microwave processing generally requires a substantially lower temperature than in a conventional furnace. This suggests some physical effects in the wave-powder interactions aside from the rapid volumetric heat deposition. The understanding of these effects is of importance to the full realization of this promising technology. Thermally activated particle bonding and inter-particle neck growth are key densification processes in both conventional and microwave sintering. The present study shows that the attractive force is intrinsic to the latter method. The force density and total force are derived in analytical forms and numerically evaluated. Results show that their strength is significant enough to play a constructive role in particle bonding and neck growth.

Keywords: Microwave; Dielectric material sintering; Induced polarization charges; Gap electric field intensification; Attractive electric force

Introduction

We begin with a brief background of microwave sintering, in particular, the general observation of a lower processing temperature than conventional sintering and the interpretations proposed thus far. Sintering is by far the most-widely used thermal processing technique for the densification of fine powders into desired materials [1], with the furnace as the prevalent heat source. The advent of the microwave oven in the 1960s has initiated the field of microwave sintering in anticipation of its potential advantages. As reviewed in different stages of the research [2-8], a wide range of materials have since been successfully sintered by microwaves under a variety of conditions. Versus the surface absorption in a furnace, the volumetric nature of microwave heating offers the advantages of rapid heating, reduced processing temperature/time, and lower energy consumption. The vast majority of experiments use the 2.45 GHz microwave. Even more rapid heating has been demonstrated with millimeter waves [2,9,10]. There are, however, also problems found in some studies, such as thermal runaways and sample fractures [11-16]. To date, this method still needs to be better characterized and controlled for broader industrial acceptance.

Following decades of research, further advances of the microwave approach call for a better understanding of the fundamental mechanisms involved. The basic theory of microwave heating has been well documented (see, for example, Refs. [2-4]).

For example, volumetric heat deposition leads to rapid heating. However, treatments by the microwave and furnace exhibit a major difference not yet fully understood. Numerous experiments have shown that microwave sintering requires a significantly reduced processing temperature [2-8,17-22]. For example, Brosnan et al. conducted a comparative study on microwave and conventional sintering of alumina. The samples reached 95% density by microwave heating at a temperature of 1,350 ℃, ~250 ℃ lower than by conventional heating [17]. The lack of clear reasons for the difference suggests some non-thermal effects (also called microwave effects) produced specifically by the electromagnetic fields (see, for example, Refs. [3-6]). While still an open subject, some explanations have been proposed by researchers, of which the ponderomotive diffusion mechanism (discussed below) has been well recognized.

A series of theoretical and experimental investigations [23-25] have shown that, during microwave heating of ceramic or glass materials, the microwave ponderomotive force in the vicinity of boundary surfaces can be sufficiently strong to cause mobile ion transport in solids, hence an enhanced mass transport and reaction rate.

By switching on and off the microwave in a hybrid microwave/conventional furnace, Wroe and Rowley demonstrated a lower sintering temperature with microwave heating [26]. They theorized that the enhanced sintering is due to the space charge induced by the microwave field on the grain boundary, which preferentially increases the driving force for grain boundary transport. The magnetic field is also shown to be beneficial in cases involving magnetic materials or an applied magnetic field [27,28]. The polarization current and the wave magnetic field inside a dielectric particle may also cause an inward magnetic force [29].

A University of Maryland group has shown in theory that, by applying a microwave to two neighboring dielectric spheres, a much greater E-field can be induced in the gap region [30]. The authors theorize that the intensified gap field may lead to ponderomotive diffusion and plasma generation, hence resulting in a higher mass transfer rate. Qiao and Xie have also shown, by simulation and experiment, that the high temperature caused by E-field intensification leads to fusing of solid materials and enhances the mass transportation [31].

The electric field intensification effect has also been applied elsewhere. For example, the intensified E-field between carbon particles can cause a chemical reaction [32] or discharge [33]. E-field intensification between two catalyst particles in a solvent has been studied in connection with microwave-assisted chemical synthesis [34,35]. As has been recently shown, the same effect is behind the household puzzle of grape sparks in a microwave oven [36,37].

The non-thermal effect in microwave sintering is still an important issue for further understanding. Here we present a rather different candidate in the form of the attractive force between two sintered particles due to their intensified gap E-field. We anticipate that, as in Ref. [30], the microscopic interaction between a pair of particles can shed light on the macroscopic behavior of a complex system of fine particles under microwave radiation. Section II examines the physics of polarization charge buildup and the resulting gap E-field intensification. Sec. III derives the attractive force between two dielectric spheres in a rigorous manner. Section IV discusses the significance of the attractive force on microwave sintering of power compacts. A summary is presented in Sec. V.

Polarization-Charge Effects Between Two Dielectric Spheres in an External Electric Field

Polarization-charge enhancement and gap electric field intensification in a DC electric field

Consider two identical dielectric spheres aligned on the x-axis with permittivity ε, radius R, and gap distance d [Figure 1(a)]. For a simulation study of the polarization-charge effects, we first apply a uniform static electric field $E_{ext}\mathbf{e}_x$, where $\mathbf{e}_x$ is a unit vector along the common axis of the two spheres Simulations here and subsequently are performed with either Ansys Maxwell (for static cases) or HFSS (for high-frequency cases), both solving the full set of Maxwell equations by the finite element method. Perfectly matched layers (PMLs) are used on a closed boundary, which absorb the electromagnetic fields acting on it.

Figure 1(a) shows the E-field pattern for two well-separated spheres with $\varepsilon/\varepsilon_0 = 20$ and $d/R = 2$, where ε_0 is the permittivity of free space. There is negligible coupling between the spheres, so the solution is found to be essentially that for a single sphere with an induced surface polarization-charge density (σ_{pol}) and a uniform E-field inside the sphere ($E_{in}\mathbf{e}_x$) given by {Ref. [38], Eqs. (4.55) and (4.58)}.

$$\sigma_{pol} = 3\varepsilon_0\left(\frac{\varepsilon-\varepsilon_0}{\varepsilon+2\varepsilon_0}\right)E_{ext}\cos\theta \tag{1}$$

$$E_{in} = \frac{3E_{ext}}{\varepsilon/\varepsilon_0+2}, \tag{2}$$

Equation (1) is applicable to the z = 0 plane in which θ is the angle between the x-axis and the observation direction. In Eq. (1), σ_{pol} is symmetric about the x-axis, positive on the right half of the spherical surface ($0<\theta<\pi/2$) and negative on left half ($\pi/2<\theta<\pi$) with a maximum $|\sigma_{pol}|$ at $\theta = 0$ and π. The E_{in} in Eq. (2) is much reduced from E_{ext} (for the large $\varepsilon/\varepsilon_0$ used) due to the shielding by the induced $\pm\sigma_{pol}$. Note that the solutions in Eqs (1) and (2) are independent of R.

The $\pm\sigma_{pol}$ produce a pure dipole E-field outside the sphere {Ref. [38], Eqs. (4.54)}, with decreasing strength away from the sphere. At a smaller gap distance, $d/R = 0.4$ [Figure 1(b)], a significant dipole field from one sphere penetrates into the other sphere to polarize some of its molecules, and vice versa. This leads to mutual enhancement of polarization charges on the surfaces facing the gap. As d narrows further, stronger and stronger polarization-charge field of one sphere enters the other, leading to further $\pm\sigma_{pol}$ enhancement and hence a much higher gap E-field.

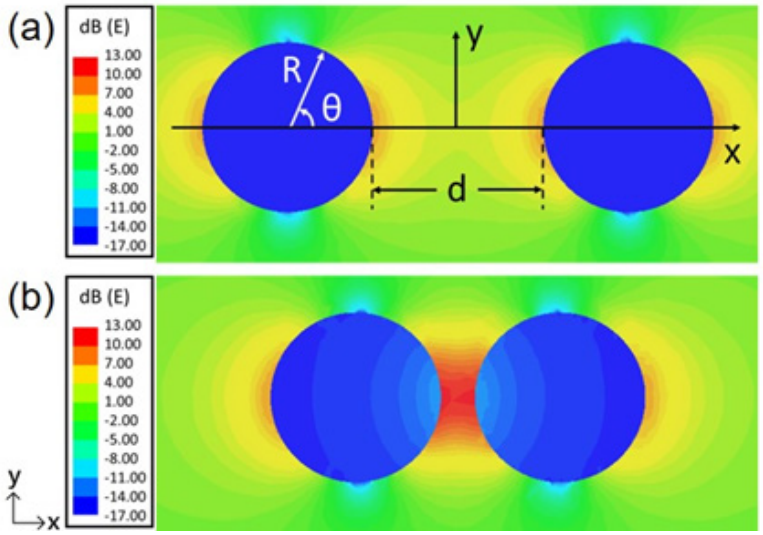

Figure 1: An illustration of the polarization-charge buildup and gap E-field intensification between two identical dielectric spheres in a uniform static E-field: $E_{ext}\mathbf{e}_x$. The dielectric constant is $\varepsilon/\varepsilon_0 = 20$, sphere radius is R, and gap distance is d. The x-y plane cuts through the centers (at z = 0) of the two spheres. (a) The field pattern for $d/R = 2$; (b) The field pattern for $d/R = 0.4$. The color code gives the electric field (normalized to E_{ext}) in logarithmic scale.

Quasi-static regime under microwave radiation

Figure 2(a) shows the same two spheres as in Figure 1 separated by a much shorter distance ($d/R<<1$). Instead of exposure to a static E_{ext} as in Figure 1, the spheres are now radiated by a 2.45 GHz plane wave linearly-polarized in the x-direction and propagating downward in the $-\mathbf{e}_y$ direction. The wavelength in the dielectric is $\lambda_d = \lambda_{free}/\mathrm{Re}(\varepsilon/\varepsilon_0)^{1/2}$, where λ_{free} is the free space wavelength (12.25 cm at 2.45 GHz). Under the condition:

$$R << \lambda_d \text{ (quasi-static regime)} \quad (3)$$

The region in and around the spheres belongs to the near zone, where E_{ext} is instantaneously uniform. The induced fields are thus dominated by a quasi-static electrical component with a spatial dependence well approximated by that of the static equations (Ref. [38], Sec. 10.1). In this regime, all fields oscillate in-phase with E_{ext}.

As a check of this limit, we assume a real ε since the smaller imaginary part has a negligible effect on the conclusion. Denote the E-field in the gap region by E_{gap}. Figure 2(b) plots E_{gap} (x = y = 0)/ E_{ext} as functions of R for $\varepsilon/\varepsilon_0 = 20$ (hence $\lambda_d = 2.74$ cm) and different values of d/R. It can be seen that the field is essentially independent of R for a fixed d/R up to $R \approx 0.5$ cm (the borderline of the quasi-static regime).

The quasi-static regime is satisfied for practically all micro-sized particles for sintering. Hence, data in this regime is applicable to a broad parameter space via the following simplifications: 1. The results are essentially independent of the incident wave frequency; 2. For configurations with fixed relative dimensions (e.g., same d/R), lengths are normalizable to R and E-fields normalizable to E_{ext}; and 3. The gap magnetic field, reflection, scattering (included in the simulation) are negligibly small. Beyond the quasi-static regime, electromagnetic resonances start to take place in the spheres [36].

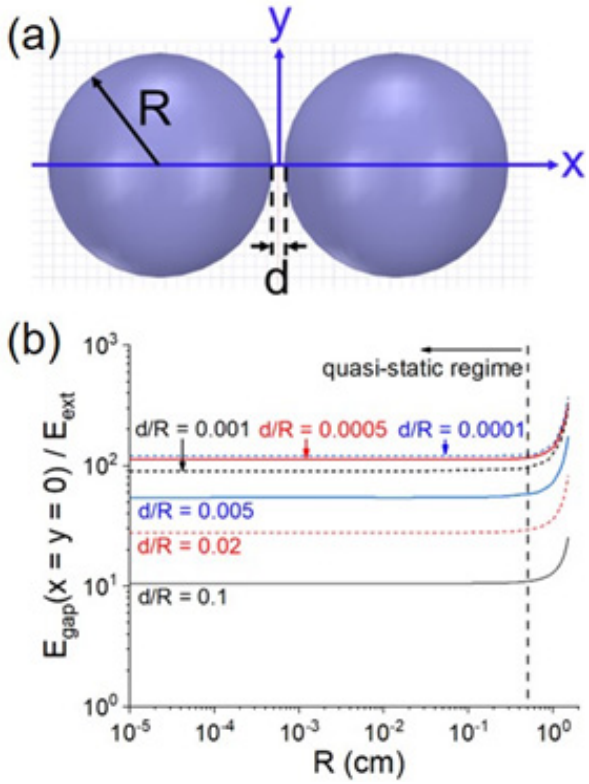

Figure 2: Validity check of the quasi-static regime. (a) Two closely spaced identical dielectric spheres with $\varepsilon/\varepsilon_0 = 20$, radius R, and separation d are shown on the z = 0 plane with the x-axis being their common axis. The two spheres are under a downward 2.45 GHz incident plane wave linearly polarized in the x-direction. (b) E_{gap} (x = y = 0)/ E_{ext} as functions of R for different values of d/R. Note that E_{gap} (x = y = 0)/ E_{ext} converges as $d/R \to 0$.

Electric field profiles in the quasi-static regime

In the quasi-static regime, the representative E-field pattern under the model in Figure 2(a) is plotted in Figure 3(a). Figure 3(b)

shows the E-field profiles (normalized to E_{ext}) along the x-axis for several values of d/R. It can be seen in Figure 3(b) that E_{gap} (x, y = 0) is relatively constant along the x-axis within the gap, with a maximum of E_{gap} (x = y = 0)/ E_{ext} =10.5, 28, and 55 for d/R =0.1, 0.02, and 0.005, respectively. In contrast, the profiles of E_{gap} (x = 0, y) along the y-axis [Figure 2(c)] drops sharply away from y = 0 with a half-maximum half width of 0.35R, 0.17R, and 0.10R for d/R = 0.1, 0.02, and 0.005, respectively. Along both the x- and y-axes, the E_{gap} features a narrow spatial extent, indicating the localized nature of the intensified E-field in the gap region.

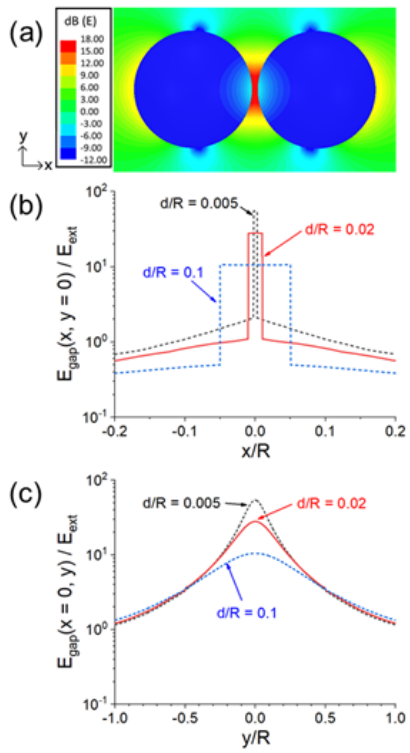

Figure 3: An illustration of the intensified E_{gap} between two closely spaced spheres with $\varepsilon/\varepsilon_0$ = 20, radius R, and variable separation d. The spheres are under a downward 2.45 GHz incident plane wave with E_{ext} linearly polarized in the x-direction. (a) E-field pattern for d/R = 0.1 on the x-y plane, which cuts through the centers (at z = 0) of the two spheres. The color code gives the electric field (normalized to E_{ext}) in logarithmic scale. (b) Profiles of E_{gap} (x, y = 0)/ E_{ext} along the x-axis for d/R = 0.005, 0.02, and 0.1. (c) Profiles of E_{gap} (x= 0, y)/ E_{ext} along the y-axis for d/R = 0.005, 0.02, and 0.1.

Figure 4(a) shows two spheres connected by a circular neck of diameter ℓ. Except for the neck, the surfaces are spherical. In this case, $\pm\sigma_{pol}$ can still build up on opposite sides of the gap around the neck. This is because polarization charges are bound to their respective molecules, hence not free to move between the spheres to neutralize each other. Under a downward 2.45 GHz incident plane wave linearly polarized in the x-direction, the E-field pattern for ℓ/R = 0.4 is shown in Figure 4(b) and the E-field profiles (normalized to E_{ext}) along the y-axis [E (x = 0, y)] is shown in Figure 4(c) for different values of ℓ/R. The E-field has a maximum at the periphery of the neck (x=0, y =± ℓ/2).

For both the closely spaced and connected spheres, the E_{gap} reduces significantly with an increasing gap separation d/R [Figs. 3(b) and 3(c)] or neck diameter ℓ/R [Figure 4(b)]. The reductions are for different reasons. The E_{ext} $\boldsymbol{e}_x$ induces a $-\sigma_{pol}$ on the left half and a $+\sigma_{pol}$ on right half of each sphere. The mutually enhanced $\pm\sigma_{pol}$ on the gap surfaces produce the intensified E_{gap}, while the oppositely oriented $\pm\sigma_{pol}$ on the outer surfaces produce an E-field to partially cancel the E_{gap}. The cancellation effect is minimal for the closely spaced spheres. The reduction of E_{gap} for a larger d/R is due to weaker enhancement of $\pm\sigma_{pol}$ on the gap surfaces.

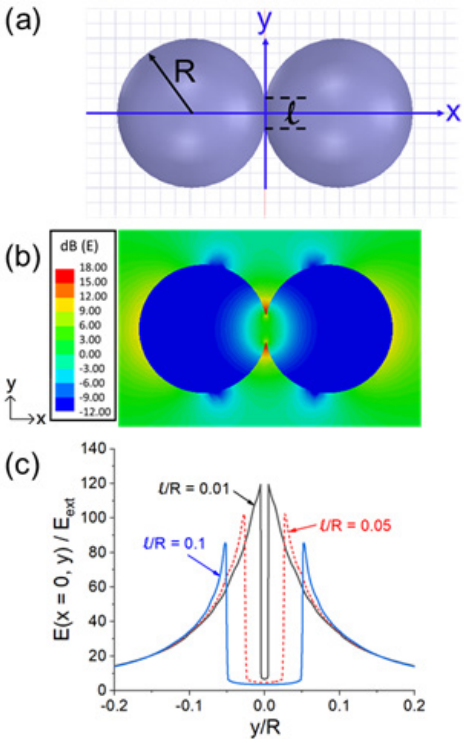

Figure 4: An illustration of intensified E_{gap} between two connected spheres. (a) Two dielectric spheres with $\varepsilon/\varepsilon_0$ = 20 and radius R with a variable neck diameter ℓ are exposed to a downward 2.45 GHz incident plane wave with E_{ext} linearly polarized in the x-direction. (b) The E-field pattern for ℓ/R = 0.4 on the x-y plane, which cuts through the centers (at z = 0) of the two spheres. The color code gives the electric field (normalized to E_{ext}) in logarithmic scale. (c) Profile of E (x = 0, y) along the y-axis for ℓ/R = 0.01, 0.05, and 0.1.

However, for the connected spheres, two different effects account for the reduction of E_{gap} with ℓ/R. First, a greater ℓ/R implies a shorter distance between the $\pm\sigma_{pol}$ on the outer surfaces, thus a more appreciable cancellation of the E_{gap}. Second, a larger ℓ/R also implies less surface areas across the gap to accommodate the $\pm\sigma_{pol}$, hence a smaller E_{gap}. These two effects are more pronounced at a higher $\varepsilon/\varepsilon_0$, which leads to a more rapid drop of E_{gap} with ℓ/R (as will be shown in Figure 7 below).

Attractive Force Due to Intensified Gap Electric Field in the Quasi-Static Regime

Force density on the spherical surface

The presence of a highly intensified gap E-field and the strong $\pm\sigma_{pol}$ on opposite sides of the gap suggests a considerable attractive

force between the spheres. The force on one sphere mirrors that on the other. So, we consider only the left sphere in spherical coordinates, using the x-axis (instead of the commonly used z-axis) as the zenith direction with r = 0 being the center of the left sphere, where r is the radial coordinate [see Figure 5(a)]. By symmetry, the quasi-static fields and electrical potential are independent of the azimuthal angle φ; hence $E_\varphi = 0$ and the surface charge σ_{pol} (at $r = R$) depends only on the polar angle θ.

The force per unit area on the surface is not simply given by $\sigma_{pol}\mathbf{E}$ because the self-field of a charge does not exert a force on itself. Excluding the self-field which causes an E-field discontinuity at $r = R$, the effective E-field ($\mathbf{E}_{eff}$) that actually exerts a force on σ_{pol} is one half of the sum of the E-fields on both sides of the $r = R$ surface [39]:

$$\mathbf{E}_{eff}(R,\theta) = \frac{1}{2}\left[\mathbf{E}(R^-,\theta) + \mathbf{E}(R^+,\theta)\right] \quad (4)$$

where $R^\pm = R \pm\delta$ with $\delta\to 0$. The self-field of σ_{pol} (R, θ) is perpendicular to the surface; hence, only $E_r(R^-, \theta)$ and $E_r(R^+, \theta)$ are different while E_θ is continuous across $r = R$. Thus,

$$\mathbf{E}_{eff}(R,\theta) = \frac{1}{2}[E_r(R^-,\theta) + E_r(R^+,\theta)]\mathbf{e}_r + E_\theta(R,\theta)\mathbf{e}_\theta \quad (5)$$

where er is a unit vector along the radial coordinate. Since there is no free charge, the perpendicular electrical displacement ($D_r = \varepsilon_0 E_r$ in free space; $D_r = \varepsilon E_r$ in the sphere) is continuous, which dictates a sharp discontinuity in E_r [e.g., Figure 3(c)]:

$$E_r(R^-,\theta) = E_r(R^+,\theta)\frac{\varepsilon_0}{\varepsilon} \quad (6)$$

Equations (5) and (6) give

$$\mathbf{E}_{eff}(R,\theta) = \frac{E_r(R^+,\theta)}{2}\left(1+\frac{\varepsilon_0}{\varepsilon}\right)\mathbf{e}_r + E_\theta(R,\theta)\mathbf{e}_\theta \quad (7)$$

Applying the boundary condition on E_r (Gauss law) and using Eq. (6), we obtain

$$\left(1-\frac{\varepsilon_0}{\varepsilon}\right)E_r(R^+,\theta) = \frac{\sigma_{pol}(R,\theta)}{\varepsilon_0}, \quad (8)$$

or

$$\sigma_{pol}(R,\theta) = \varepsilon_0\left(1-\frac{\varepsilon_0}{\varepsilon}\right)E_r(R^+,\theta) \quad (9)$$

In the quasi-static regime, σ_{pol}, E_r, and E_θ all oscillate in phase. So, the time-averaged force density (force per unit area) is

$$\left\langle \mathbf{f}(R,\theta)\right\rangle_t = \left\langle \sigma_{pol}(R,\theta)\mathbf{E}_{eff}\right\rangle_t$$
$$= \frac{1}{4}\varepsilon_0\left(1-\frac{\varepsilon_0^2}{\varepsilon^2}\right)E_r^{2,\text{peak}}(R^+,\theta)\mathbf{e}_r + \frac{1}{2}\varepsilon_0\left(1-\frac{\varepsilon_0}{\varepsilon}\right)E_r^{peak}(R^+,\theta)E_\theta^{peak}(R,\theta)\mathbf{e}_\theta \quad (10)$$

where the superscript "peak" refers to the peak value (in time) of the respective symbol. Note that, under condition (3), E_r and E_θ are proportional to E_{ext}, and are functions of the normalized parameter d/R or ℓ/R.

Denote the r and θ-components of the force density in Eq. (10) by $\langle f_r(R, \theta)\rangle_t$ and $\langle f_\theta(R, \theta)\rangle_t$, respectively. Their profiles in the full range of θ ($0<\theta<\pi$) are illustrated in Figure 5 in physical unit for an incident field of E_{ext} (peak) =200 V/cm (typical peak field of a loaded household microwave oven [40]). The force densities in Figure 5 are for two closely spaced spheres with $\varepsilon/\varepsilon_0 = 20$ and $d/R = 0.02$. Values are symmetrical about the x-axis, with a sharp and narrow peak of $\langle f_r(R, \theta)\rangle_t$ at $\theta \approx 0$. Figure 6 is the counterpart of Figure 5 for two connected spheres with $\varepsilon/\varepsilon_0 = 20$ and $\ell/R = 0.2$. In Figure 6(b), there is no force for $\theta<\theta_n$, where θ_n is the polar angle of the periphery of the neck. As in Figure 5, there is a sharp and narrow peak of $\langle f_r(R, \theta)\rangle_t$ at $\theta \approx \theta_n$.

Figures 5 and 6 illustrate in general that the spatial maxima of the force density (with respect to θ) occur at $\theta = 0$ and θ_n for closely spaced and connected spheres, respectively. The spatial maxima, denoted by $\langle f(R, \theta=0)\rangle_t$ and $\langle f(R, \theta=\theta_n)\rangle_t$, are plotted in physical unit as continuous functions of d/R [Figure 7(a)] and ℓ/R [Figure 7(b)], for E_{ext} (peak) = 200 V/cm and $\varepsilon/\varepsilon_0 = 5$, 10, and 20. In both Figure 7(a) and 7(b), the force densities for $\varepsilon/\varepsilon_0 = 20$ peak at ~130 dyne/cm^2. The corresponding E-field is ~2.5×10^4 V/cm, which is just below the air breakdown strength of 3×10^4 V/cm at 1 atm [41]. So, this is approximately the maximum force density without invoking an air breakdown at 1 atm. For lower values of $\varepsilon/\varepsilon_0$, E_{ext} (peak) can be tuned upward to reach this maximum value.

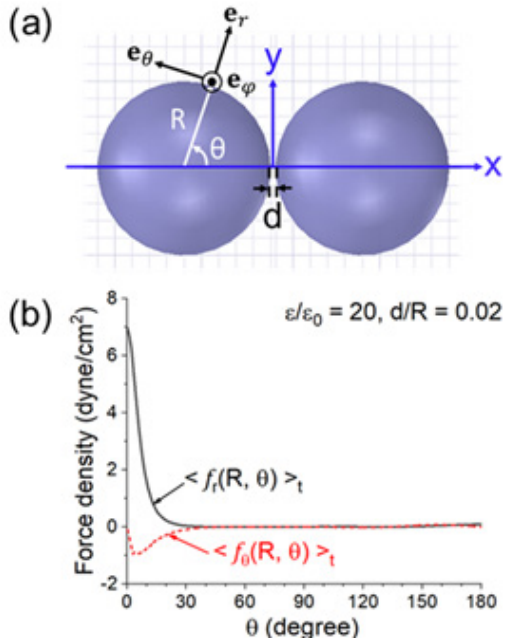

Figure 5: An illustration of the force density in physical unit for two closely spaced spheres under E_{ext} (peak) = 200 V/cm (typical of a loaded household microwave oven [40]). (a) Two closely spaced spheres on the x-axis separated by distance d and plotted on the x-y plane, which cuts through the centers (at z = 0) of the two spheres. Spherical coordinates are shown with r = 0 being the center of the left sphere. (b) Profiles of $\langle f_r(R, \theta)\rangle_t$ and $\langle f_\theta(R, \theta)\rangle_t$ on the left sphere as functions of θ for $\varepsilon/\varepsilon_0 = 20$ and $d/R = 0.02$.

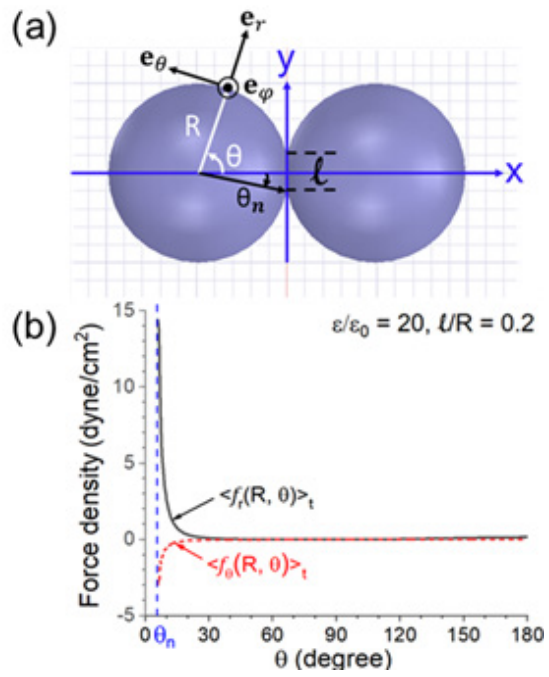

Figure 6: An illustration of the force density in physical unit for two connected spheres under E_{ext} (peak) = 200 V/cm. (a) The configuration for two connected spheres with a neck diameter ℓ/R plotted on the x-y plane, which cuts through the centers (at z = 0) of the two spheres. Spherical coordinates are shown with r = 0 being the center of the left sphere. (b) Profiles of $<f_r(R, \theta)>_t$ and $<f_\theta(R, \theta)>_t$ as functions of θ for $\varepsilon/\varepsilon_0$ = 20 and ℓ/R = 0.2.

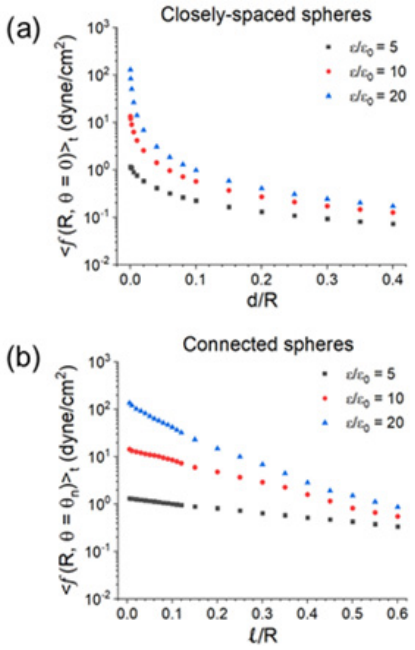

Figure 7: Maximum magnitude of the force density (with respect to θ) in physical unit for E_{ext} (peak) = 200 V/cm and $\varepsilon/\varepsilon_0$ = 5, 10, and 20. (a) $<f(R, \theta=0)>_t$ as functions of d/R for two closely spaced spheres. (b) $<f(R, \theta=\theta_n)>_t$ as functions of ℓ/R for two connected spheres.

Due to the finite mesh size in the simulation, the smallest calculated d/R or ℓ/R in Figure 7 is 10^{-4}, at which the two spheres are almost on single-point contact. This is the configuration for which the force density reaches an absolute maximum for the respective $\varepsilon/\varepsilon_0$. The absolute maxima converge to the same value as d/R or $\ell/R \to 0$, indicating a continuous transition from separation, point contact, to connection. The force density data spans a wide range in the parameter space. It decreases sharply with a greater d/R or ℓ/R. In particular, for two connected spheres, the force density decreases more rapidly for a larger $\varepsilon/\varepsilon_0$ for the reasons discussed in connection with Figure 4. However, the region of interest to sintering (e.g., powder compaction and neck growth) lies in the lower ranges of d/R and ℓ/R, where the force densities approach the highest values.

Total attractive force between two spheres

The total attractive force between two closely spaced spheres is in the x-direction by symmetry [under condition (3)]. The x-component of the force density $<f(R, \theta)>_t$ in Eq. (10) is

$$\begin{aligned}\left\langle f_x(R,\theta)\right\rangle_t &= \left\langle \mathbf{f}(R,\theta)\right\rangle_t \cdot \mathbf{e}_x \\ &= \frac{1}{4}\varepsilon_0\left(1-\frac{\varepsilon_0^2}{\varepsilon^2}\right)E_r^{2,\text{peak}}(R^+,\theta)\cos\theta \\ &\quad -\frac{1}{2}\varepsilon_0\left(1-\frac{\varepsilon_0}{\varepsilon}\right)E_r^{\text{peak}}{}_r(R^+,\theta)E_\theta^{\text{peak}}(R,\theta)\sin\theta \end{aligned} \quad (11)$$

A surface integral then gives the total attractive force

$$\left\langle F_x(R,\theta)\right\rangle_t = \oint_s \left\langle f_x(R,\theta)_t\right\rangle da = 2\pi R^2 \int_0^\pi \left\langle f_x(R,\theta)\right\rangle_t \sin\theta d\theta \quad (12)$$

where da is a differential surface area. The E_{gap} is greatest when the incident wave is polarized in the x-direction, which is the most favorable direction for polarization-charge enhancement across the gap [36]. A randomly polarized E_{ext} (as in a microwave oven) will make the average force isotropic, but approximately halve the value in Eqs. (10)-(12).

In Figure 5, we find that the force density is dominated by the peak at $\theta \approx 0$, which is predominantly a radially outward force proportional to the square of E_r. Hence, the total force is always attractive independent of the field direction.

The total force is extremely small on a micro-sized sphere because the surface area is proportional to R^2. On the other hand, the total mass in the sphere is proportional to R^3. So, the attractive force actually produces a greater acceleration on a smaller sphere. In terms of the accelerating effect, a useful figure of merit is the force on a unit volume of the sphere, which we define as

$$\frac{\text{force}}{\text{unit volume}} = \frac{\text{total force on sphere}}{\text{volume of sphere}} = \left(\frac{3}{4\pi R^3}\right)\left\langle F_x(R,\theta)\right\rangle_t \quad (13)$$

Figure 8 shows the attractive force per unit volume for two closely spaced spheres as a function of R for E_{ext} (peak) = 200 V/cm and different values of d/R and $\varepsilon/\varepsilon_0$. As in Figure 7, all E-fields are below the air breakdown strength at 1 atm. Consider, for example, two spheres with R = 1 μm, $\varepsilon/\varepsilon_0$ = 20, and d/R = 0.001. The attractive force per unit volume is ~5×10^3 dyne/cm³. If the sphere has a specific weight of 2.5, its frictionless acceleration will be

2×10^3 cm/sec^2, which is about twice the gravitational acceleration. The acceleration is greater (weaker) for smaller (larger) spheres. In a vacuum medium or an ambient gas with a higher dielectric strength, greater acceleration can be achieved at a larger E_{ext}. The significance of the electric force will be discussed next in Sec. IV.

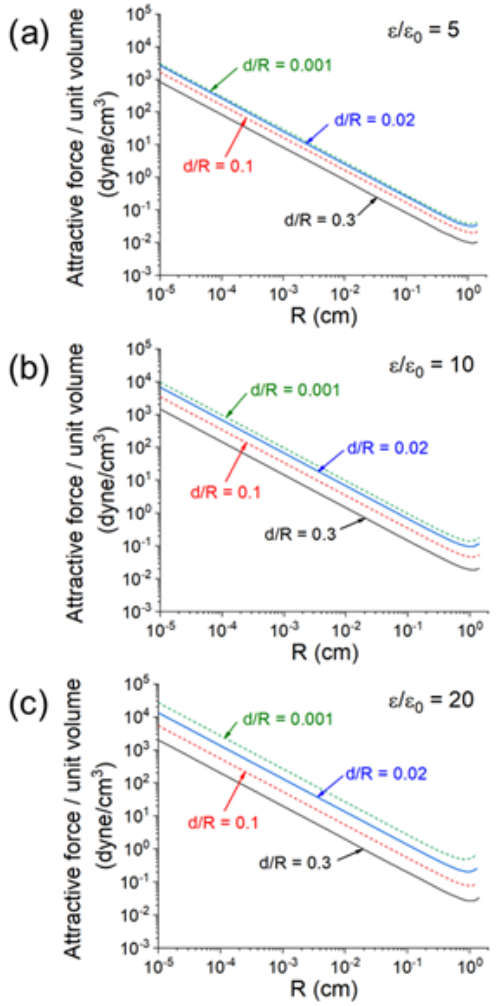

Figure 8: Attractive force per unit volume on each of two closely spaced spheres shown in Figure 5(a) as a function of R for E_{ext} (peak) = 200 V/cm and several values of d/R. (a) $\varepsilon/\varepsilon_0$ = 5, (b) $\varepsilon/\varepsilon_0$ = 10, and (c) $\varepsilon/\varepsilon_0$ = 20. The quasi-static regime applies to R<<0.5 cm, beyond which electromagnetic resonances take place in the spheres.

Potential Significance to Microwave Sintering

As discussed in detail in Ref. [1], the primary process for matter transport in sintering is thermally activated diffusion of atoms, ions, or molecules, which results in bonding and neck formation. A variety of paths are involved in this process including lattice, grain boundary, and surface diffusion. Several effects of a non-thermal nature have been proposed to explain the lower processing temperature in microwave sintering (discussed in Sec. I). Here we present arguments on the viability of the electric force as a non-thermal effect.

In Sec. III, we have shown that the electric force is always attractive between two neighboring dielectric spheres. It is a microscopic, non-contact force considerably different from the contact force of an externally applied pressure. The starting powder for sintering is commonly assumed to be a compacted mass of spherical particles. Assume two particles, 1 μm in radius and 2.5 in specific weight, are nearly in touch and exposed to E_{ext}(peak)=200 V/cm (typical of a household microwave oven). According to Figure 8, the attractive force can cause a frictionless acceleration up to a few g (=980 cm/sec^2) without an air breakdown at 1 atm. Compared with powder compaction by gravitational or centrifugal settling [1], the electric force can be made isotropic in a multimode, randomly polarized microwave cavity to achieve a more compact state.

As an inter-particle neck forms and grows, the force keeps acting in the gap around the newly formed neck, reaching a strength over 100 dyne/cm^2 [Figure 7(b)] without an air breakdown. Its persistent presence may thus assist the densification process by promoting the neck growth, particularly in the liquid phase (discussed below).

Liquid-phase sintering does not have to be conducted above the melting temperature of the major sample under treatment. A small number of additives can be mixed with the major component to remedy the problem of inadequate densification. The commonly used additives (SiO_2, CaO, MgO, SrO, BaO, La_2O_3, Y_2O_3, and TiO_2) have a dielectric constant of 2 (SiO_2) to 60 (TiO_2) [42]. They melt on the surfaces of major particles, which often significantly enhances the mass transport. For example, densification of ~1% La_2O_3/BaO-doped ZST ceramic can be completed at 1350 ℃, ~275 ℃ lower than the un-doped case [43]. In fact, according to a recent review [8], over 70% of sintered products are formed using the liquid phase, which constitutes 90% of the commercial sintered product value.

The driving force for sintering is the reduction in free energy of the consolidated system [1]. This is commonly accomplished by, for example, atomic diffusion which leads to body densification by matter transport into the pores. Similar considerations suggest the tendency of surface bonding by the attractive force across a high E_{gap} [Figure 7(b)], thereby releasing the E-field energy. The surface tension may also play a facilitating role in that the neck growth leads to a reduction of the surface area, hence a lower surface energy state.

Interestingly, there appears to be a strong correlation between the current theory and an early experimental study focusing on orientational effects. In sintering the doped $BaTiO_3$ PTCR materials heated to 1,250 ℃ by a linearly polarized microwave, Chang and Jian found a strong orientational dependence of the sample shrinkage rates and grain growth [44]. The maximum shrinkage is 48% along the E-field as compared to 26% in the perpendicular direction. The sintered grains also show an E-field oriented strip-

like microstructure. No clear reason was identified by the authors. However, the directional coincidence between these effects and maximum polarization-charge buildup suggests the attractive force as a plausible cause. Considering the complexity of the sintering process, more experimental evidence are apparently needed to draw a definitive conclusion. Theoretically, it is also of interest to develop a multiple-grain model to find out how the attractive force can affect mass transport via the vacancy diffusion process.

Conclusion

We have presented a detailed theory on the electric attractive force between two dielectric spheres under microwave radiation. This is an inter-particle force inherent in microwave sintering of powder compacts, a method known to require a substantially lower processing temperature than conventional sintering for reasons still under investigation. The attractive force acts on the gap surfaces between two sintering particles nearly in touch (Figure 5) or connected by a neck (Figure 6). These are the regions where the primary sintering process takes place, and the attractive forces concentrate. As quantitatively illustrated in Figure 7(b) and 8, the force has a significant strength to play a supplemental role in particle bonding and neck growth normally achieved by thermally activated atomic diffusion. There is a dearth of literature on the effects of the E-field orientation in microwave sintering. The current theory, however, provides an explanation for an early sintering experiment, which found much greater sample shrinkage and a strip-like microstructure in the direction of the wave electric field. Hopefully, the formalism and data base presented here could be a useful reference for a more definitive investigation.

The theory may also be applicable elsewhere. For example, in a stormy cloud, the collision and coalescence of water droplets (typical $R \approx 10$ μm) are the primary mechanism for the formation of rain drops (typical $R \approx 1$ mm) [45]. The water droplets often exist in a high E-field produced by atmospheric charges. The attractive forces between droplets in close encounters can thus enhance the collision cross-section. If the intensified E-field before the collision exceeds the air breakdown strength, a discharge between two droplets can become additional source of atmospheric charges.

Acknowledgement

The authors are grateful to ANSYS, Inc. for generously providing the Maxwell and HFSS software used throughout this research and to Dr. H. H. Teng for helpful technical assistance. This work was funded by the Ministry of Science and Technology, Taiwan, under Grant No. MOST 110-2112-M-002-019.

Conflict of Interest

No conflict of Interest.

Reference

1. MN Rahaman (2017) Ceramic Processing and Sintering. 2nd Edition, Taylor & Francis Group, New York.
2. JD Katz (1992) Microwave sintering of ceramics. Annu Rev Mater Sci 22: 153-170.
3. DE Clark, WH Sutton (1996) Microwave processing of materials. Annu Rev Mater Sci 26: 299-331.
4. M Oghbaei, O Mirzaee (2010) Microwave versus conventional sintering: A review of fundamentals, advantages and applications. J Alloys Compd 494: 175-189.
5. ZZ Fang (2010) Sintering of advanced materials. (First Edition) Woodhead Publishing Limited, Sawston, England.
6. KI Rybakov, EA Olevsky, EV Krikun (2013) Microwave sintering: fundamentals and modeling. J Am Ceram Soc 96(4): 1003-1020.
7. M Bhattacharya, T Basak (2016) Susceptor-assisted enhanced microwave processing of ceramics - a review. Crit Rev Solid State Mater Sci 42(4): 433-469.
8. L Ćurković, R Veseli, I Gabelica, I Žmak, I Ropuš, et al. (2021) A review of microwave-assisted sintering technique. Trans Famena 45(1): 256786.
9. AW Fliflet, RW Bruce, RP Fischer, D Lewis, LK Kurihara, et al. (2000) A study of millimeter-wave sintering of fine-grained alumina compacts. IEEE Trans Plasma Sci 28(3): 924-935.
10. IN Sudiana, R Ito, S Inagaki, K Kuwayama, K Sako, et al. (2013) Densification of alumina ceramics sintered by using sub-millimeter wave gyrotron. J Infra Milli Terahertz Waves 34: 627-638.
11. GA Kriegsmann (1992) Thermal runaway in microwave heated ceramics A one-dimensional model. J Appl Phys 71(4): 1960.
12. MS Spotz, DJ Skamser, DL Johnson (1995) Thermal Stability of Ceramic Materials in Microwave Heating. J Am Ceram Soc 78(4): 1041-1048.
13. CA Vriezinga, S Sanchez-Pedreno, J Grasman (2002) Thermal runaway in microwave heating: a mathematical analysis. Appl Math Model 26(11): 1029-1038.
14. RR Menezes, PM Souto, RHGA Kiminami (2012) Microwave fast sintering of ceramic materials. Sintering of Ceramics – New Emerging Techniques, Edited by A. Lakshmanan Intech Open, London, England.
15. X Cheng, C Zhao, H Wang, Y Wang, Z Wang (2020) Mechanism of irregular crack-propagation in thermal controlled fracture of ceramics induced by microwave. Mech Ind 21(6): 610.
16. T Garnault, D Bouvard, JM Chaix, S Marinel, C Harnois (2021) Is direct microwave heating well suited for sintering ceramics? Ceramics International 47(12): 16716-16729.
17. KH Brosnan, GL Messing, DK Agrawal (2003) Microwave sintering of alumina at 2.45 GHz. J Am Ceram Soc 86(8): 1307-1312.
18. A Chanda, S Dasgupta, S Bose, A Bandyopadhyay (2009) A Microwave sintering of calcium phosphate ceramics. Mater Sci Eng C 29(4): 1144-1149.
19. P Figiel, M Rozmus, B Smuk (2011) Properties of alumina ceramics obtained by conventional and nonconventional methods for sintering ceramics. J Achiev Mater Manuf Eng 48(1): 29-34.
20. J Croquesela, D Bouvard, J Chaix, CP Carry, S Saunier, et al. (2016) Direct microwave sintering of pure alumina in a single mode cavity: Grain size and phase transformation effects. Acta Mater 116: 53-62.
21. M Shukla, S Ghosh, N Dandapat, AK Mandal, VK Balla (2016) Comparative study on conventional sintering with microwave sintering and vacuum sintering of Y_2O_3-Al_2O_3-ZrO_2 ceramics. J Mater Sci Chem Eng 42(2): 71-78.

22. S Ramesh, N Zulkifli, CY Tan, YH Wong, F Tarlochan, et al. (2018) Comparison between microwave and conventional sintering on the properties and microstructural evolution of tetragonal zirconia. Ceram Int 44(8): 8922-8927.

23. KI Rybakov, VE Semenov (1994) Possibility of plastic deformation of an ionic crystal due to the nonthermal influence of a high-frequency electric field. Phys Rev B Condens Matter 49(1): 64-68.

24. SA Freeman, JH Booske, RF Cooper (1995) Microwave field enhancement of charge transport in sodium chloride. Phys Rev Lett 74(11): 2042-2045.

25. JH Booske, RF Cooper, SA Freeman, KI Rybakov, VE Semenov (1998) Microwave ponderomotive forces in solid-state ionic plasmas. Phys Plasmas 5: 1664.

26. R Wroe, AT Rowley (1996) Evidence for a non-thermal microwave effect in the sintering of partially stabilized zirconia. J Materials Sci 31: 2019-2026.

27. A Badev, R Heuguet, S Marinel (2013) Induced electromagnetic pressure during microwave sintering of ZnO in magnetic field. J Eur Ceram Soc 33(6): 1185-1194.

28. Y Xiao, F Xu, B Dong, W Liu, X Hu (2017) Discussion on the Local Magnetic Force between Reversely Magnetized Micro Metal Particles in the Microwave Sintering Process. Metals 7(2): 47.

29. F Xu, B Dong, X Hua, Y Wang, W Liu, et al. (2016) Discussion on magnetic-induced polarization Ampere's force by in situ observing the special particle growth of alumina during microwave sintering. Ceram Int 42(7): 8296-8302.

30. A Birnboim, JP Calame, Y Carmel (1999) Microfocusing and polarization effects in spherical neck ceramic microstructures during microwave processing. J Appl Phys 85: 478-482.

31. X Qiao, X Xie (2016) The effect of electric field intensification at interparticle contacts in microwave sintering. Sci Rep 6: 32163.

32. JA Menéndez, EJ Juárez-Pérez, E Ruisánchez, JM Bermúdez, A Arenillas (2011) Ball lightning plasma and plasma arc formation during the microwave heating of carbons. Carbon 49(1): 346-349.

33. M Liu, L Zhang, W Zhou, J Gao, P Wang, et al. (2020) The mechanism of microwave-induced discharge between submillimeter active coke. Plasma Sources Sci Technol 29(7): 075015.

34. S Horikoshi, A Osawa, S Sakamoto, N Serpone (2013) Control of microwave-generated hot spots. Part V. Mechanisms of hot-spot generation and aggregation of catalyst in a microwave-assisted reaction in toluene catalyzed by Pd-loaded AC particulates. Appl Catal A: General 460-461: 52-60.

35. Haneishi, S Tsubaki, E Abe, MM Maitani, E Suzuki, et al. (2019) Enhancement of fixed-bed flow reactions under microwave irradiation by local heating at the vicinal contact points of catalyst particles. Sci Rep 9: 222.

36. MS Lin, LC Liu, LR Barnett, YF Tsai, KR Chu (2021) On electromagnetic wave ignited sparks in aqueous dimers. Phys Plasmas 28: 102102.

37. E Siegel (2021) Sparks fly when you microwave grapes: here's the science of why. Big Think.

38. JD Jackson (1998) Classical Electrodynamics (Third Edition). John Wiley, New York.

39. DJ Griffiths (2013) Introduction to Electrodynamics. (Fourth Edition), Pearson Education, Boston.

40. J Monteiro, LC Costa, MA Valente, T Santos, J Sousa (2011) Simulating the electromagnetic field in microwave ovens. in SBMO/IEEE MTT-S International Microwave and Optoelectronics Conference (IMOC 2011), Natal. IEEE, Piscataway, New Jersey, pp. 493-497.

41. D Halliday, J Walker, R Resnick (2014) Fundamentals of Physics, (Tenth Edition), Wiley, Hoboken, New Jersey.

42. AA Demkov, A Navrotsky (2005) Materials Fundamentals of Gate Dielectric. Springer, Dordrecht, Netherlands.

43. SX Zhang, JB Li, HZ Zhai, JH Dai (2002) Low temperature sintering and dielectric properties of $(Zr_{0.8}Sn_{0.2})$ TiO_4 microwave ceramics using La_2O_3/BaO additives. Mater Chem Phys 77(2): 470-475.

44. A Chang, J Jian (2003) The orientation growth of grains in doped $BaTiO_3$ PTCR materials by microwave sintering. J Mater Proc Tech 137: 100-101.

45. HR Pruppacher, JD Klett (2010) Microphysics of Clouds and Precipitation. Springer, New York.